Article

Signature of the western boundary currents in local climate variability

https://doi.org/10.1038/s41586-024-08019-2

Received: 19 April 2024

Accepted: 3 September 2024

Published online: 02 October 2024

Check for updates

James G. Larson[1], David W. J. Thompson[1,2]✉ & James W. Hurrell[1]

The western boundary currents are characterized by narrow, intense ocean jets and are among the most energetic phenomena in the world ocean. The importance of the western boundary currents to the mean climate is well established: they transport vast quantities of heat from the subtropics to the midlatitudes[1], and they govern the structure of the climatological mean surface winds[2–6], precipitation[4–6] and extratropical storm tracks[7–13]. Their importance to climate variability is much less clear, as the tropospheric response to extratropical sea surface temperature (SST) variability is generally modest relative to the internal variability in the midlatitude atmosphere[12–14]. Here we exploit novel local analyses based on high-spatial-resolution data to demonstrate that SST variability in the western boundary currents has a more robust signature in climate variability than has been indicated in previous work. Our results indicate that warm SST anomalies in the major boundary currents of both hemispheres are associated with a distinct signature of locally enhanced precipitation and rising motion anomalies that extend throughout the depth of the troposphere. The tropospheric signature closely mirrors that of ocean dynamical processes in the boundary currents. Thus, the findings indicate a distinct and robust pathway through which extratropical ocean dynamical processes influence local climate variability. The observational relationships are also reproducible in Earth system model simulations but only when the simulations are run at high spatial resolution.

The oceanic western boundary currents have a robust influence on the climatological mean atmospheric circulation. They are marked by large spatial gradients in the climatological mean sea surface temperature (SST) field that influence the development of baroclinic eddies[7–13], the horizontal structure of the near-surface flow[2–6] and the climatological distribution of precipitation and clouds[4–6].

The influence of the western boundary currents on atmospheric variability is less clear. Ocean mesoscale eddies in the vicinity of major ocean currents have a distinct signature in the surface winds and precipitation[15,16], but whether this effect extends to monthly variations in the atmospheric flow is unclear. A central issue in detecting a robust response to SST variability across the western boundary currents is that the large-scale atmospheric response to extratropical SST variability is often weak relative to the internal climate variability. Hence, although some previous numerical and observational studies have reported a robust atmospheric response to SST variability in the western boundary currents[9,17–23], the responses vary depending on the spatial scale and location of the SST variability, the seasonally varying structure of the atmospheric flow and various aspects of the analysis design[12–14,24]. As noted in the seminal 2002 review led by Yochanan Kushnir, 'the extratropical ocean does indeed influence the atmosphere outside of the boundary layer, but … this influence is of modest amplitude compared to internal atmospheric variability'[14]. Likewise, the more recent review by Arnaud Czaja et al. states, 'While the recent research provides more optimism for a source of predictability from the ocean than was available at the time of the review by Kushnir et al.[14], several outstanding issues remain'[12]. These issues include robustness across models, reproducible observational benchmarks and regional sensitivity of the responses.

Here we demonstrate that the primary western boundary current regions of both hemispheres have a distinct but overlooked signature in atmospheric variability that mirrors the complex structure of the underlying SST field. The novel aspect of the analyses that facilitates the key finding is that they are based on the covariability between fine-spatial-resolution atmospheric vertical motion, precipitation and SST anomalies at the grid point level, whereas previous studies have emphasized the covariability between various atmospheric fields and SSTs averaged over larger spatial regions.

The primary high-spatial-resolution observational data are SSTs, vertical motion and precipitation data from the European Centre for Medium-Range Weather Forecasts (ECMWF) Reanalysis v.5 available at 0.25° × 0.25° resolution (ERA5); in situ and remotely sensed SST data from the National Oceanic and Atmospheric Administration (NOAA) Daily Optimum Interpolation SSTs dataset available at 0.25° × 0.25° resolution (DOISST v.2.0); and remotely sensed precipitation data from the Integrated Multi-satellite Retrievals for the Global Precipitation Measurement (IMERG) of the National Aeronautics and Space Administration (NASA) product available at 0.1° × 0.1° resolution. The precipitation data are filtered in the space domain with a 1,000-km spatial high-pass filter to reduce the signature of synoptic and planetary-scale

[1]Department of Atmospheric Science, Colorado State University, Fort Collins, CO, USA. [2]School of Environmental Sciences, University of East Anglia, Norwich, UK. ✉e-mail: david.thompson@colostate.edu

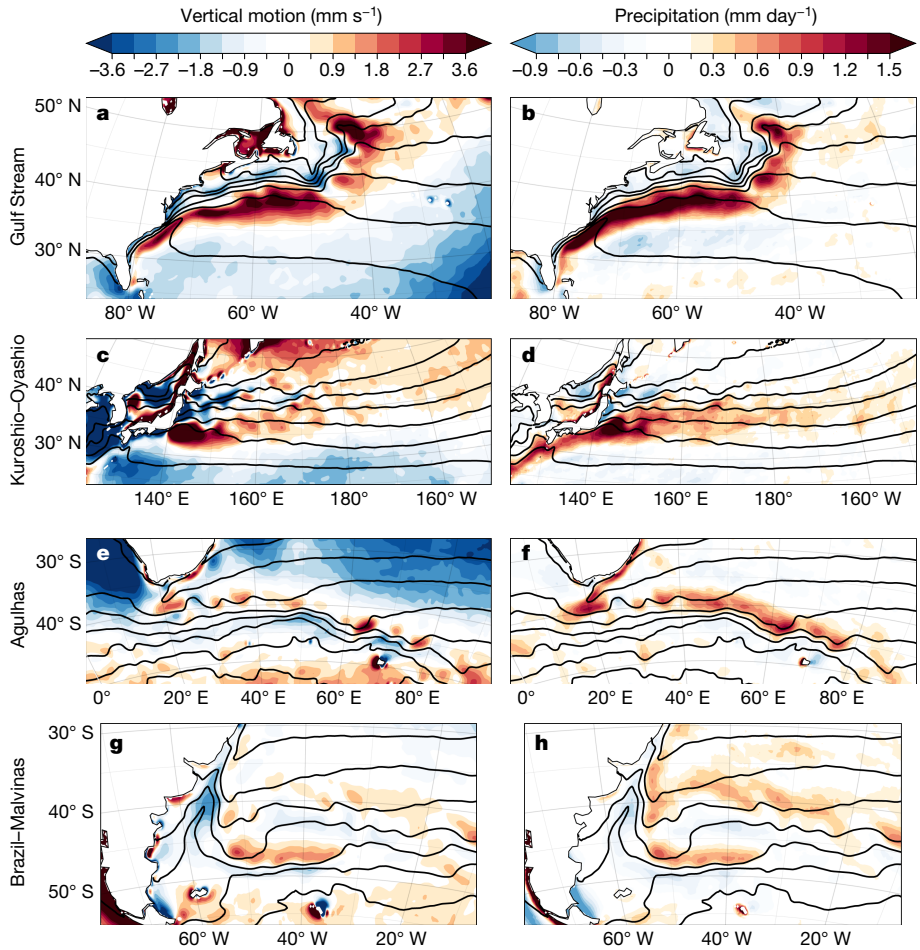

Fig. 1 | Observed signature of the western boundary currents in climatological mean vertical motion and precipitation. a–h, The wintertime mean of SSTs (contours) overlaid with the mean atmospheric vertical motion at 850 hPa (**a**,**c**,**e**,**g**) and spatially high-pass-filtered precipitation (**b**,**d**,**f**,**h**). The vertical motion is smoothed with a 3-point (about 75 km) spatial running mean for display purposes only. Contours range from 275 K to 296 K at increments of 3 K. The rows correspond to the four western boundary currents of interest. Results are based on the ERA5 dataset.

atmospheric phenomena in the precipitation field. Note that a similar high-pass filter was applied in ref. 2 for the analysis of the mean surface winds over the oceans[2]. As demonstrated below, effectively identical results are derived from analyses based on the ERA5 convective precipitation product, and qualitatively similar results are derived from analyses based on unfiltered precipitation data. In all results, we focus on the cold-season months when atmospheric variability is most vigorous: October–March in the Northern Hemisphere and April–September in the Southern Hemisphere. Further information on the datasets and analysis techniques is provided in the Methods.

Figure 1 provides a synopsis of the observed relationships between the climatological mean SST field, atmospheric vertical motion near the top of the atmospheric boundary layer (850 hPa) and precipitation over four prominent western boundary current regions: The Gulf Stream extension in the North Atlantic; the Kuroshio–Oyashio extension in the North Pacific; the Agulhas Current to the southeast of South Africa; and the Brazil–Malvinas Confluence to the east of southern South America. In all four current systems, the regions of largest horizontal SST gradients (indicated by the closely spaced contours in Fig. 1) are collocated with distinct structures in the atmospheric flow: enhanced vertical motion and precipitation are evident along the southern edge of the Gulf Stream extension[4] (Fig. 1a,b), the Kuroshio–Oyashio extension[25] (Fig. 1c,d), the northern edge of the Agulhas Current region[26] (Fig. 1e,f) and in a lobster-claw pattern that extends eastwards from the Argentinian coast near the Brazil–Malvinas Confluence (Fig. 1g,h). The regions of enhanced vertical motion are anticipated from the patterns of surface wind convergence associated with mesoscale features in the SST field[2–6]. The pattern of precipitation associated with the Gulf Stream was first noted in ref. 4 and the signature of precipitation associated with the Agulhas Current was explored in ref. 26. To our knowledge, the existence of similar patterns of precipitation anchored by the Brazil–Malvinas Confluence has not been demonstrated.

Figure 2 shows the signature of fine-scale SST variability in the western boundary currents in atmospheric variability. Figure 2a,d,g,j shows the standard deviations of the monthly mean SST anomalies during the cold-season months, in which the anomalies are defined as the departures from the long-term mean seasonal cycle (Methods). As indicated in previous works, the boundary currents are marked by distinct patterns of maxima in SST variability: the Gulf Stream extension by a strip of narrow, meandering variability that extends across the northwestern North Atlantic[27]; the Kuroshio–Oyashio current system by a more amorphous pattern that extends eastwards from Japan[28]; the Agulhas Current system by a band that stretches across nearly 80° of longitude[29]; and the Brazil–Malvinas Confluence by a lobster-claw pattern reminiscent of that evident in the mean vertical motion[30]. Similar patterns of SST variability are recovered from the high-resolution NOAA SST product (Extended Data Fig. 1a,d,g,j).

Figure 2b,e,h,k shows the covariability between SST and lower tropospheric vertical motion anomalies. As noted earlier, the results are constructed by regressing vertical motion anomalies onto SST anomalies

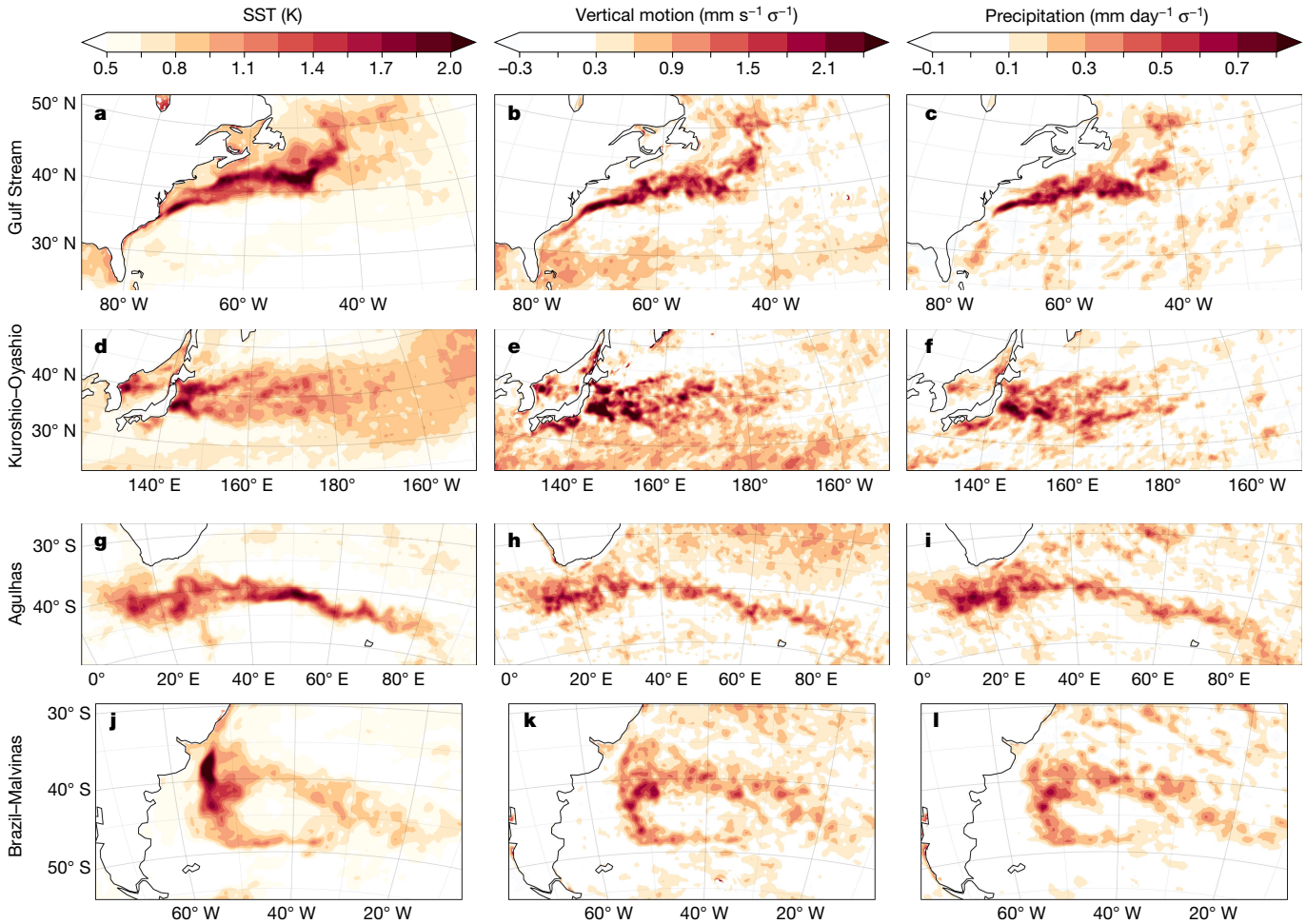

Fig. 2 | Observed signature of the western boundary currents in month-to-month variability in vertical motion and precipitation. a,**d**,**g**,**j**, The standard deviations of grid point SST anomalies. **b**,**e**,**h**,**k**, Grid point vertical motion anomalies at 850 hPa regressed onto grid point SST anomalies. **c**,**f**,**i**,**l**, Grid point precipitation anomalies regressed onto grid point SST anomalies. Anomalies are defined as departures from the long-term mean seasonal cycle (Methods). The rows correspond to the four western boundary currents of interest. Results are based on monthly mean data from ERA5.

as a function of grid point. That is, results at grid point *i* correspond to vertical motion (w_{850}) at grid point *i* regressed onto standardized values of the SST field at the same location. Red values indicate anomalous rising motion during months when SSTs are anomalously warm, and vice versa. Note that the methodology used in Fig. 2b,e,h,k contrasts that used in many previous studies, in which the regressions are based not on grid point SST but rather on SSTs averaged over broad spatial regions (for example, see refs. 21,22,31 and references therein).

In all four boundary current regions, months characterized by anomalously high SSTs are associated with anomalous rising motion. The most pronounced vertical motion anomalies closely mirror the structure of variability in the underlying SST field, with monthly anomalies exceeding 1 mm s^{-1} over the regions of the largest SST variability in all current regions. The close correspondence between the patterns of covariability between vertical motion and SST anomalies (Fig. 2b,e,h,k) and variability in the SST field (Fig. 2a,d,g,j) is striking in association with all boundary currents. The main features in Fig. 2b,e,h,k are statistically significant (Extended Data Fig. 2a,c,e,g), and the results are reproducible in analyses based on the high-resolution NOAA SST product (Extended Data Fig. 1b,e,h,k). Over the core of the current regions, month-to-month variability in the SST field accounts for up to 20–30% of the month-to-month variability in lower tropospheric vertical motion (Extended Data Fig. 3).

The variations in vertical motion associated with grid point SST variability are not limited to the lower troposphere. Figure 3 shows the local regression coefficients between vertical motion and SST anomalies, calculated as a function of vertical level 900–200 hPa, and then spatially averaged over the four respective current regions. Figure 3a shows the spatial average of the regression coefficients based on grid point SST variability, rather than the regression coefficients based on spatially averaged SSTs. The spatial averaging is performed over all grid boxes in which the regressions in Fig. 3a exceed 0.8 mm s^{-1} σ^{-1} at 850 hPa (the masks used in the spatial average are indicated in Extended Data Fig. 4). Figure 3b indicates the corresponding *P*-values found using a one-tailed test of the *t*-statistic and the corresponding number of temporal degrees of freedom (Methods). The vertical motion anomalies associated with a 1 standard deviation change in SSTs exceed the 95% confidence level into the middle troposphere in all four regions (Fig. 3b). The depth and sign of the vertical motion anomalies suggest that the anomalous surface fluxes associated with western boundary current SST variability drive perturbations in the atmospheric flow that extend through the middle troposphere. The depth of the signature of the western boundary currents in vertical motion is another new aspect of the results.

Figure 2c,f,i,l shows the associated linkages between precipitation and SST variability. The precipitation results shown in Fig. 2 are based on ERA5 for consistency with the vertical motion field. Similar results are derived by regressing the IMERG remotely sensed precipitation product onto the NOAA SST product (Extended Data Fig. 1c,f,i,l). As evidenced by comparing the three columns in Fig. 2, SST variability in all four western boundary current systems projects onto precipitation variability in a manner consistent with the attendant changes in vertical motion.

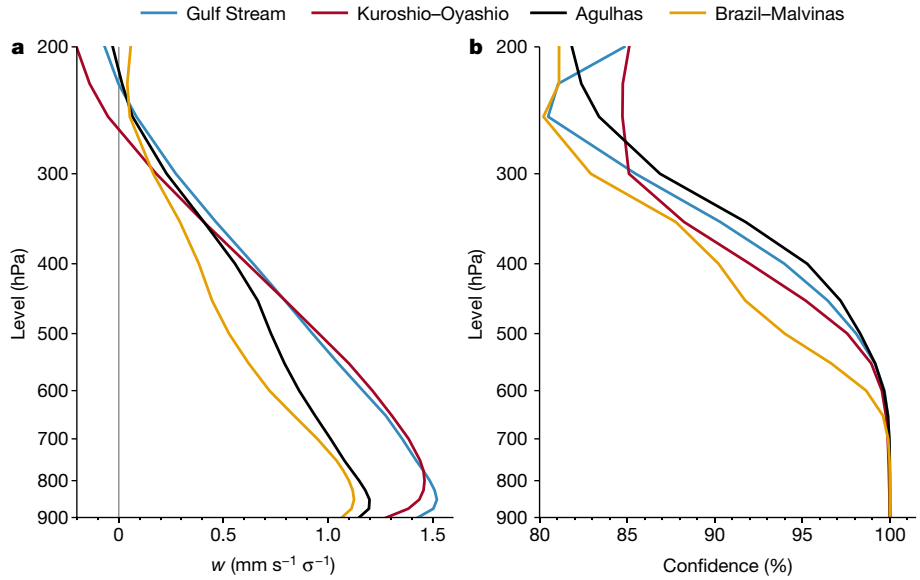

Fig. 3 | Vertical motion variability associated with SST variability in the four western boundary current regions. a, Vertical profiles of the area-average of grid point regressions between vertical motion and SST anomalies for the indicated regions (the spatial masks used to define the regions are shown in Extended Data Fig. 4). **b**, The associated confidence level based on a Student's *t*-test using 88 degrees of freedom. See the Methods for more details. Results are based on ERA5.

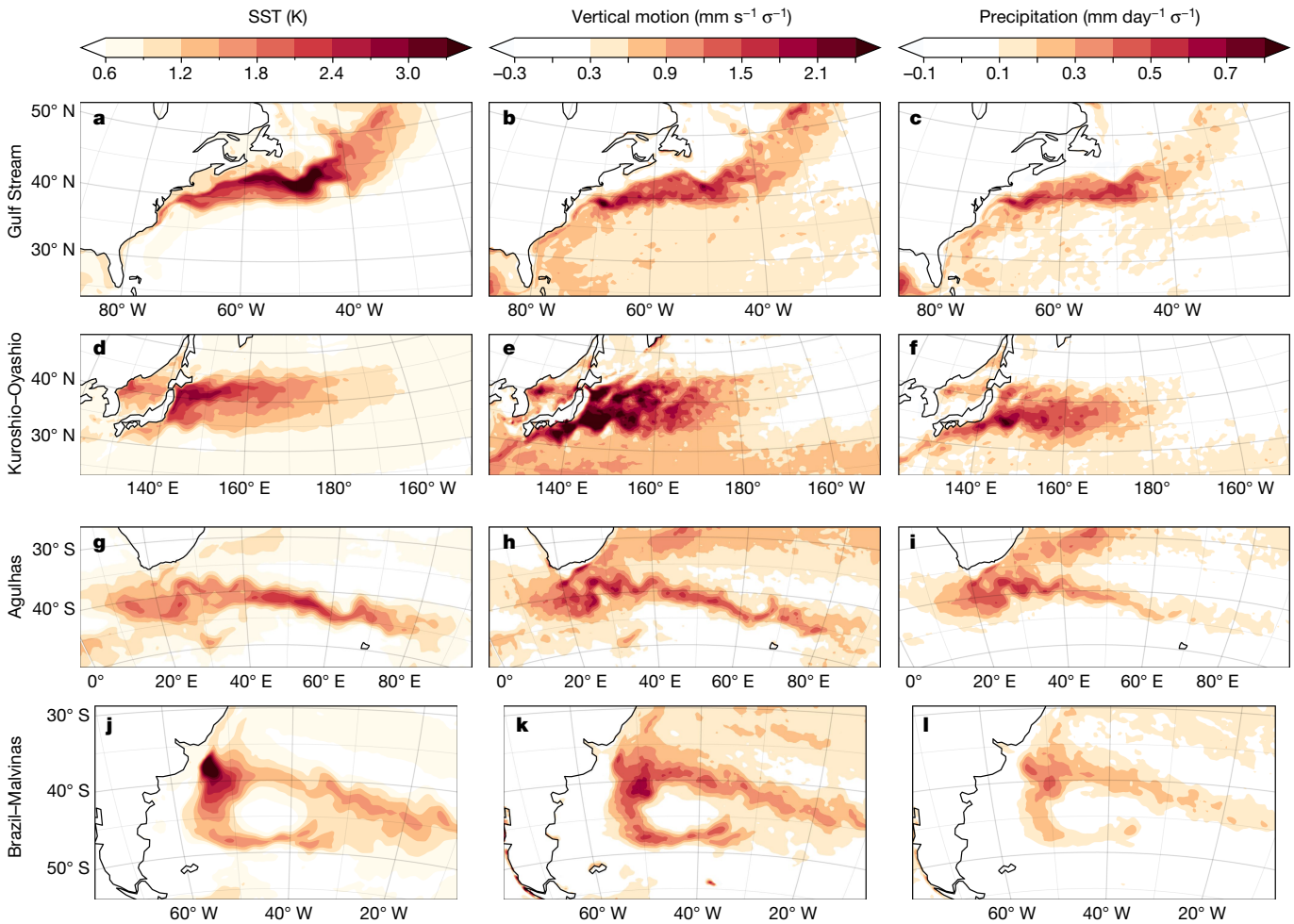

Fig. 4 | Simulated signature of the western boundary currents in a high-resolution coupled atmosphere–ocean global climate model. a,**d**,**g**,**j**, The standard deviations of grid point SST anomalies. **b**,**e**,**h**,**k**, Grid point vertical motion anomalies at 850 hPa regressed onto grid point SST anomalies. **c**,**f**,**i**,**l**, Grid point precipitation anomalies regressed onto grid point SST anomalies. The rows correspond to the four western boundary currents of interest. Results are based on monthly mean output from experiments run under the auspices of the iHESP project on a high-resolution version of the CESM. The atmospheric resolution is 0.25°; the ocean resolution is 0.1°.

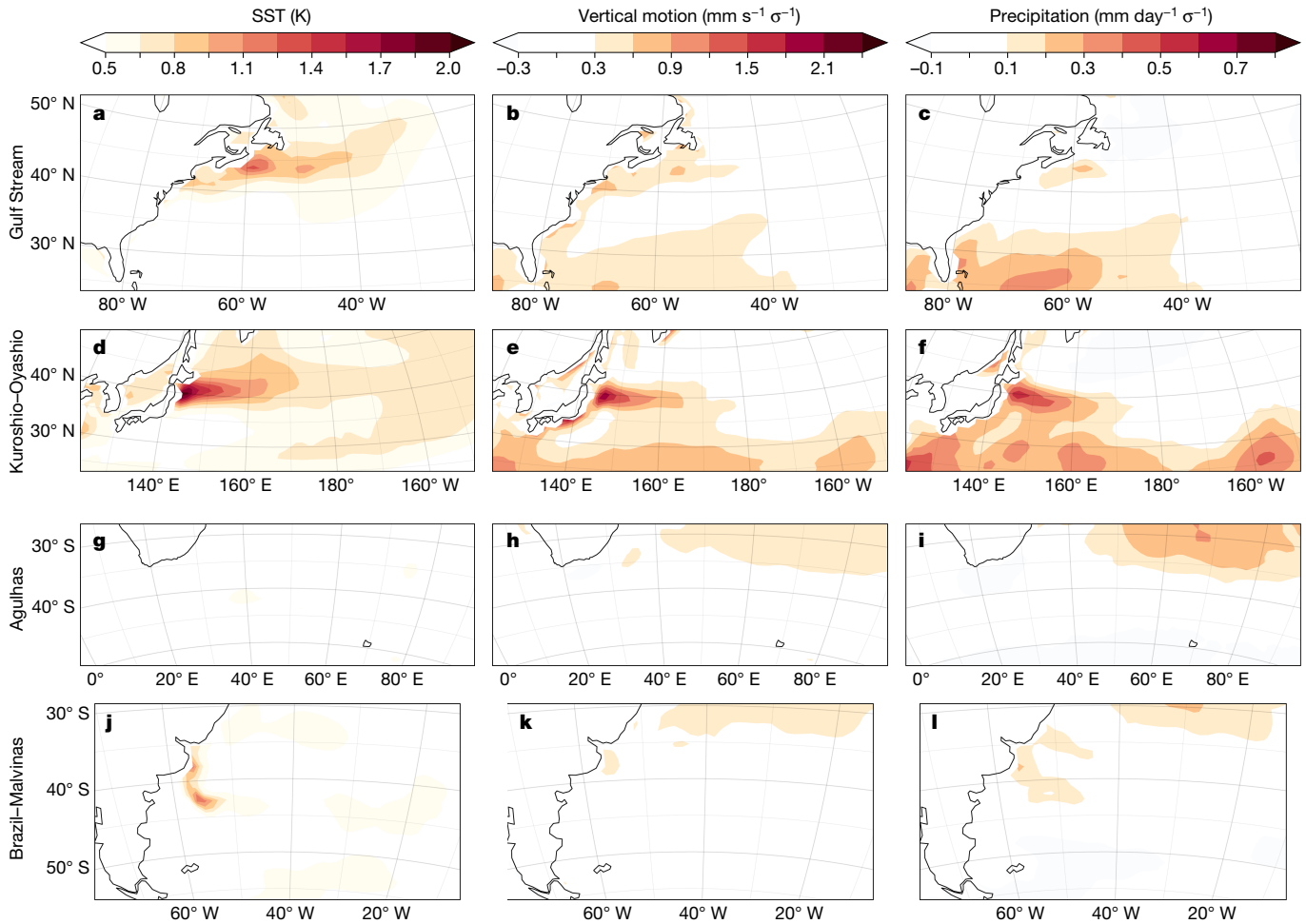

Fig. 5 | Simulated signature of the western boundary currents in a low-resolution coupled atmosphere–ocean global climate model. a,**d**,**g**,**j**, The standard deviation of grid point SST anomalies. **b**,**e**,**h**,**k**, Grid point vertical motion anomalies at 850 hPa regressed onto grid point SST anomalies. **c**,**f**,**i**,**l**, Grid point precipitation anomalies regressed onto grid point SST anomalies. The rows correspond to the four western boundary currents of interest. Results are based on monthly mean output from experiments run under the auspices of the iHESP project on a low-resolution version of the CESM. The atmospheric and ocean resolution is 1.0°.

Months when local SSTs are anomalously high are associated with locally enhanced precipitation anomalies, and vice versa. The primary features are statistically significant (Extended Data Fig. 2b,d,f,h), explain roughly 20–30% of the month-to-month variance in precipitation (Extended Data Fig. 3b,d,f,h), are almost identical to those derived from analyses based on the ERA5 convective precipitation product (Extended Data Fig. 5b,e,h,k) and are readily apparent in analyses based on precipitation data that has not been spatially filtered (Extended Data Fig. 5c,f,i,l).

The key finding in Fig. 2 is that the spatial patterns of atmosphere–ocean coupling over the western boundary currents closely mirror the spatial patterns of the SST variability itself. The observed linkages between the SST field, vertical motion and precipitation are also reproducible in numerical simulations run at high spatial resolution. Figures 4 and 5 show the same results as that of Fig. 2, but for output from two 250-year preindustrial control simulations run on a coupled atmosphere–ocean global climate model: a high-resolution simulation run at an atmospheric resolution of 0.25° and an ocean resolution of 0.1° and a relatively low-resolution simulation run at an atmospheric and ocean resolution of approximately 1°. The simulations were run using the Community Earth System Model (CESM) under the auspices of the International Laboratory for High-Resolution Earth System Prediction (iHESP) project (Methods). The patterns of simulated SST variability in the high-resolution simulations are strikingly similar to those found in observations (compare the left columns of Figs. 2 and 4).

The covariability between vertical motion, precipitation and SST variability are likewise simulated by the high-resolution CESM across all western boundary currents, including over the unique lobster-claw pattern of SST maxima associated with the Brazil–Malvinas Confluence system and the zonally elongated pattern of SST maxima associated with the Agulhas Current (compare the middle and right columns in Figs. 2 and 4). Notably, the robust patterns of covariability over the western boundary currents are largely absent in the low-resolution simulation (Fig. 5). Overall, the reproducibility of the relationships in a numerical model run at high resolution attests to the robustness of the results over a much longer period of record and the ability of a high-resolution coupled model to simulate the observed covariability. Consistent with earlier reports[19,32], the differences between Figs. 4 and 5 highlight the importance of high spatial resolution for simulating the vertical motion response to variations in the extratropical SST field.

The physical processes that link the climatological mean SST field to the atmospheric circulation include a range of meso- and synoptic-scale phenomena[13]. For example, in the long-term mean, regions of relatively high extratropical SSTs are marked by locally enhanced precipitation not only during the passage of atmospheric frontal systems[33–36] but also due to perturbations in surface pressure and vertical mixing that can arise in the absence of frontal passages[34,37–39]. The close correspondence between the structure of atmosphere–ocean interactions in the long-term mean (as shown in previous work) and in the context of

month-to-month variability (as shown here) suggests that a similarly diverse range of physical processes act to couple SST variability to the overlying circulation on both timescales. The signature of the SST field in monthly mean precipitation arises from changes in daily-mean precipitation across a range of amplitudes, which further suggests that a variety of physical processes underlie the relationships observed on month-to-month timescales (Extended Data Fig. 6).

The complex structures of SST variability in the western boundary currents are largely driven by ocean dynamical processes[28,40–45]. Hence the patterns of covariability between grid point variability in the SST field and the overlying atmosphere indicated here may be interpreted as the extratropical tropospheric response to ocean dynamical processes. The depth of the atmospheric response is important. Linear theory indicates that lower tropospheric heating anomalies are generally balanced by vertical motion in the tropics but by horizontal temperature advection in the extratropics[46]. As such, the heating associated with tropical SST anomalies is readily communicated to the mid-upper troposphere where the resulting circulation anomalies can be communicated over vast distances[46,47], whereas the heating associated with extratropical SST anomalies is more readily balanced by local circulation anomalies that are restricted to the lower troposphere[14,46]. The depth of the extratropical atmospheric features indicated here is reminiscent of that typically found in association with tropical SST anomalies; this suggests that SST variability in the western boundary currents may drive variations in the upper tropospheric circulation over regions far removed from the SST forcing. The amplitude of the remote response will depend on the spatial coherence of the precipitation variability. The spatial coherence of the local precipitation response and the resulting non-local signature in the atmospheric circulation is a focus of ongoing research.

Online content

Any methods, additional references, Nature Portfolio reporting summaries, source data, extended data, supplementary information, acknowledgements, peer review information; details of author contributions and competing interests; and statements of data and code availability are available at https://doi.org/10.1038/s41586-024-08019-2.

1. Imawaki, S., Bower, A. S., Beal, L. & Qiu, B. in *International Geophysics* Vol. 103, 305–338 (Elsevier, 2013).
2. Chelton, D. B., Schlax, M. G., Freilich, M. H. & Milliff, R. F. Satellite measurements reveal persistent small-scale features in ocean winds. *Science* **303**, 978–983 (2004).
3. O'Neill, L. W., Chelton, D. B., Esbensen, S. K. & Wentz, F. J. High-resolution satellite measurements of the atmospheric boundary layer response to SST variations along the Agulhas return current. *J. Clim.* **18**, 2706–2723 (2005).
4. Minobe, S., Kuwano-Yoshida, A., Komori, N., Xie, S.-P. & Small, R. J. Influence of the Gulf Stream on the troposphere. *Nature* **452**, 206–209 (2008).
5. Minobe, S., Miyashita, M., Kuwano-Yoshida, A., Tokinaga, H. & Xie, S.-P. Atmospheric response to the Gulf Stream: seasonal variations. *J. Clim.* **23**, 3699–3719 (2010).
6. Chelton, D. & Xie, S.-P. Coupled Ocean-Atmosphere Interaction at Oceanic Mesoscales. *Oceanography* **23**, 52–69 (2010).
7. Hoskins, B. J. & Valdes, P. J. On the existence of storm-tracks. *J. Atmos. Sci.* **47**, 1854–1864 (1990).
8. Nakamura, H., Sampe, T., Tanimoto, Y. & Shimpo, A. in *Geophysical Monograph Series* (eds Wang, C. et al.) 329–345 (American Geophysical Union, 2004).
9. Nakamura, H., Sampe, T., Goto, A., Ohfuchi, W. & Xie, S.-P. On the importance of midlatitude oceanic frontal zones for the mean state and dominant variability in the tropospheric circulation. *Geophys. Res. Lett.* **35**, 2008GL034010 (2008).
10. Woollings, T., Hoskins, B., Blackburn, M., Hassell, D. & Hodges, K. Storm track sensitivity to sea surface temperature resolution in a regional atmosphere model. *Clim. Dyn.* **35**, 341–353 (2010).
11. Hu, D. et al. Pacific western boundary currents and their roles in climate. *Nature* **522**, 299–308 (2015).
12. Czaja, A., Frankignoul, C., Minobe, S. & Vannière, B. Simulating the midlatitude atmospheric circulation: what might we gain from high-resolution modeling of air-sea interactions? *Curr. Clim. Change Rep.* **5**, 390–406 (2019).
13. Seo, H. et al. Ocean mesoscale and frontal-scale ocean–atmosphere interactions and influence on large-scale climate: a review. *J. Clim.* **36**, 1981–2013 (2023).
14. Kushnir, Y. et al. Atmospheric GCM response to extratropical SST anomalies: synthesis and evaluation. *J. Clim.* **15**, 2233–2256 (2002).
15. Frenger, I., Gruber, N., Knutti, R. & Münnich, M. Imprint of Southern Ocean eddies on winds, clouds and rainfall. *Nat. Geosci.* **6**, 608–612 (2013).
16. Liu, X., Chang, P., Kurian, J., Saravanan, R. & Lin, X. Satellite-observed precipitation response to ocean mesoscale eddies. *J. Clim.* **31**, 6879–6895 (2018).
17. Kwon, Y.-O. & Joyce, T. M. Northern Hemisphere Winter Atmospheric Transient Eddy Heat Fluxes and the Gulf Stream and Kuroshio–Oyashio Extension Variability. *J. Clim.* **26**, 9839–9859 (2013).
18. O'Reilly, C. H. & Czaja, A. The response of the Pacific storm track and atmospheric circulation to Kuroshio Extension variability. *Quart. J. R. Meteorol. Soc.* **141**, 52–66 (2015).
19. Smirnov, D., Newman, M., Alexander, M. A., Kwon, Y.-O. & Frankignoul, C. Investigating the local atmospheric response to a realistic shift in the Oyashio sea surface temperature front. *J. Clim.* **28**, 1126–1147 (2015).
20. Parfitt, R., Czaja, A., Minobe, S. & Kuwano-Yoshida, A. The atmospheric frontal response to SST perturbations in the Gulf Stream region. *Geophys. Res. Lett.* **43**, 2299–2306 (2016).
21. Wills, S. M., Thompson, D. W. J. & Ciasto, L. M. On the observed relationships between variability in Gulf Stream sea surface temperatures and the atmospheric circulation over the North Atlantic. *J. Clim.* **29**, 3719–3730 (2016).
22. Wills, S. M. & Thompson, D. W. J. On the observed relationships between wintertime variability in Kuroshio–Oyashio extension sea surface temperatures and the atmospheric circulation over the North Pacific. *J. Clim.* **31**, 4669–4681 (2018).
23. Joyce, T. M., Kwon, Y., Seo, H. & Ummenhofer, C. C. Meridional Gulf Stream shifts can influence wintertime variability in the North Atlantic storm track and Greenland blocking. *Geophys. Res. Lett.* **46**, 1702–1708 (2019).
24. Frankignoul, C., Czaja, A. & L'Heveder, B. Air–sea feedback in the North Atlantic and surface boundary conditions for ocean models. *J. Clim.* **11**, 2310–2324 (1998).
25. Tokinaga, H. et al. Ocean frontal effects on the vertical development of clouds over the western North Pacific: in situ and satellite observations. *J. Clim.* **22**, 4241–4260 (2009).
26. Nkwinkwa Njouodo, A. S., Koseki, S., Keenlyside, N. & Rouault, M. Atmospheric signature of the Agulhas current. *Geophys. Res. Lett.* **45**, 5185–5193 (2018).
27. Heiderich, J. & Todd, R. E. Along-stream evolution of Gulf Stream volume transport. *J. Phys. Oceanogr.* **50**, 2251–2270 (2020).
28. Kelly, K. A. et al. Western boundary currents and frontal air–sea interaction: Gulf Stream and Kuroshio Extension. *J. Clim.* **23**, 5644–5667 (2010).
29. Beal, L. M. & Bryden, H. L. The velocity and vorticity structure of the Agulhas Current at 32°S. *J. Geophys. Res.* **104**, 5151–5176 (1999).
30. Goni, G., Kamholz, S., Garzoli, S. & Olson, D. Dynamics of the Brazil-Malvinas Confluence based on inverted echo sounders and altimetry. *J. Geophys. Res.* **101**, 16273–16289 (1996).
31. Yook, S., Thompson, D. W. J., Sun, L. & Patrizio, C. The simulated atmospheric response to western North Pacific sea surface temperature anomalies. *J. Clim.* **35**, 3335–3352 (2022).
32. Parfitt, R., Czaja, A. & Kwon, Y.-O. The impact of SST resolution change in the ERA-Interim reanalysis on wintertime Gulf Stream frontal air-sea interaction. *Geophys. Res. Lett.* **44**, 3246–3254 (2017).
33. Parfitt, R. & Czaja, A. On the contribution of synoptic transients to the mean atmospheric state in the Gulf Stream region. *Quart. J. R. Meteorol. Soc.* **142**, 1554–1561 (2015).
34. Parfitt, R. & Seo, H. A new framework for near-surface wind convergence over the Kuroshio Extension and Gulf Stream in wintertime: the role of atmospheric fronts. *Geophys. Res. Lett.* **45**, 9909–9918 (2018).
35. Masunaga, R., Nakamura, H., Taguchi, B. & Miyasaka, T. Processes shaping the frontal-scale time-mean surface wind convergence patterns around the Gulf Stream and Agulhas return current in winter. *J. Clim.* **33**, 9083–9101 (2020).
36. Masunaga, R., Nakamura, H., Taguchi, B. & Miyasaka, T. Processes shaping the frontal-scale time-mean surface wind convergence patterns around the Kuroshio Extension in winter. *J. Clim.* **33**, 3–25 (2020).
37. Schneider, N. & Qiu, B. The atmospheric response to weak sea surface temperature fronts. *J. Atmos. Sci.* **72**, 3356–3377 (2015).
38. Schneider, N. Scale and Rossby number dependence of observed wind responses to ocean-mesoscale sea surface temperatures. *J. Atmos. Sci.* **77**, 3171–3192 (2020).
39. Small, R. J. et al. Near-surface wind convergence over the Gulf Stream—the role of SST revisited. *J. Clim.* **36**, 5527–5548 (2023).
40. Patrizio, C. R. & Thompson, D. W. J. Quantifying the role of ocean dynamics in ocean mixed layer temperature variability. *J. Clim.* **34**, 2567–2589 (2021).
41. Small, R. J., Bryan, F. O., Bishop, S. P. & Tomas, R. A. Air–sea turbulent heat fluxes in climate models and observational analyses: what drives their variability? *J. Clim.* **32**, 2397–2421 (2019).
42. Small, R. J., Bryan, F. O., Bishop, S. P., Larson, S. & Tomas, R. A. What drives upper-ocean temperature variability in coupled climate models and observations? *J. Clim.* **33**, 577–596 (2020).
43. Laurindo, L. C. et al. Role of ocean and atmosphere variability in scale-dependent thermodynamic air-sea interactions. *J. Geophys. Res. Oceans* **127**, e2021JC018340 (2022).
44. Kirtman, B. P., Perlin, N. & Siqueira, L. Ocean eddies and climate predictability. *Chaos* **27**, 126902 (2017).
45. Bishop, S. P., Small, R. J., Bryan, F. O. & Tomas, R. A. Scale dependence of midlatitude air–sea interaction. *J. Clim.* **30**, 8207–8221 (2017).
46. Hoskins, B. J. & Karoly, D. J. The steady linear response of a spherical atmosphere to thermal and orographic forcing. *J. Atmos. Sci.* **38**, 1179–1196 (1981).
47. Sardeshmukh, P. D. & Hoskins, B. J. The generation of global rotational flow by steady idealized tropical divergence. *J. Atmos. Sci.* **45**, 1228–1251 (1988).

Methods

Observations

Observations of SSTs and precipitation are obtained from the European Centre for Medium-Range Weather Forecasts (ECMWF) Reanalysis v.5 (ERA5)[48], the remotely sensed Daily Optimum Interpolation SSTs (OISST v2.1)[49] dataset of the National Oceanic and Atmospheric Administration and the remotely sensed Integrated Multi-satellite Retrievals for the Global Precipitation Measurement product (IMERG)[50] of NASA. All analyses are based on wintertime, monthly averages. A temporal subset of ERA5 from September 2007 to December 2023 was chosen because of the higher-resolution Operational Sea Surface Temperature and Ice Analysis (OSTIA)[51] SST dataset that is ingested into ERA5 during this period[48]. The OISST and IMERG datasets temporally span from January 2000 to December 2023 and from June 2006 to December 2023, respectively.

Anomalies are formed by subtracting the long-term means from the data as a function of the calendar month. The ERA5 and OISST datasets are available at 0.25° × 0.25° resolution. The IMERG product intercalibrates and interpolates several different microwave satellite measurements and is available at 0.1° × 0.1° resolution over 60° N–60° S. All data are detrended over the period 1979–2023 before the analyses to ensure trends in the data do not influence the results.

Numerical output

We analyse 250 years of wintertime, monthly mean output from 1850 preindustrial control simulation run on the Community Earth System Model v.1.3 (ref. 52) as part of the International Laboratory for High-Resolution Earth System Prediction (iHESP) project[53]. The coupled high-resolution iHESP simulations were run at atmospheric resolution of 0.25° and ocean resolution of 0.1°. The relatively high-spatial-resolution ocean model permits mesoscale eddies and thus simulates their interactions with the overlying atmosphere[53,54].

Statistics

Regression coefficients are calculated as

$$\beta = \frac{\overline{x'y'}}{\overline{x'^2}}$$

where primes denote departures from the long-term mean seasonal cycle and overbars denote the time mean. As the regressions in Figs. 2–4 are based on standardized SST data, it follows that the regression coefficients are identical to the covariances. Correlation coefficients are obtained as

$$r = \frac{\overline{x'y'}}{\sqrt{\overline{y'^2}}\sqrt{\overline{x'^2}}}.$$

The *P*-values shown in Fig. 3b are found as follows. At each vertical level, we form the spatially averaged local correlations (r^2) of SST with vertical motion over the respective western boundary current regions as

$$\bar{r} = \sqrt{\frac{1}{N}\sum_{i}^{N} r_i^2},$$

where r_i denotes the correlation at grid point i and the summation is performed over all N grid cells in the areas indicated in the text (Extended Data Fig. 4). The spatially averaged correlations are calculated separately for each vertical level.

We then estimate the number of degrees of freedom used in the correlations as

$$N^* = N\frac{1 - r_1 r_2}{1 + r_1 r_2},$$

where N is the number of time steps in the data (in this case, 6 months × 16 years = 96), and r_1 and r_2 are the grid point lag-one autocorrelations of the monthly mean SST and vertical motion fields, respectively. Owing to the large gradients in SST variability within the western boundary current regions, r_1 and r_2 vary spatially and are thus estimated by taking a masked spatial average over the regions (Extended Data Fig. 4). Using the observed r_1 and r_2 yields 88 effective degrees of freedom (N^*).

The spatially averaged correlations are then converted to *t*-scores using the relation

$$t = \bar{r}\frac{\sqrt{N^* - 2}}{\sqrt{1 - \bar{r}^2}},$$

and the *t*-scores at each level are converted to the *P*-values shown in Fig. 3b based on a one-tailed test of Student's *t*-distribution.

Additional resources

The literature on extratropical atmosphere–ocean interactions is extensive. Owing to space constraints, we are limited to 50 references in the main text. For further reading on the influence of large spatial gradients in the climatological-mean SST field on (1) storm tracks and the development of baroclinic eddies, see refs. 55–66; (2) the horizontal structure of the near-surface flow, see refs. 67–75; and (3) precipitation, see ref. 76.

Data availability

Reanalysis and observed data were obtained from ERA5 (https://cds.climate.copernicus.eu/), OISST (https://www.ncei.noaa.gov/products/optimum-interpolation-sst) and IMERG (https://gpm.nasa.gov/data/imerg). iHESP model data were obtained from https://ihesp.github.io/archive/. Base maps use freely available data from https://www.naturalearthdata.com/downloads/, plotted with the Cartopy software[77].

Code availability

The code used to process the data and produce these figures can be found at the Open Science Framework[78]. This code is licensed under the Open Software License 3.0.

48. Hersbach, H. et al. The ERA5 global reanalysis. *Quart. J. R. Meteorol. Soc.* **146**, 1999–2049 (2020).
49. Huang, B. et al. Improvements of the Daily Optimum Interpolation Sea Surface Temperature (DOISST) Version 2.1. *J. Clim.* **34**, 2923–2939 (2021).
50. Huffman, G. J. et al. in *Satellite Precipitation Measurement* (eds Levizzani, V. et al.) Vol. 67, 343–353 (Springer, 2020).
51. Donlon, C. J. et al. The Operational Sea Surface Temperature and Sea Ice Analysis (OSTIA) system. *Remote Sens. Environ.* **116**, 140–158 (2012).
52. Hurrell, J. W. et al. The Community Earth System Model: a framework for collaborative research. *Bull. Am. Meteorol. Soc.* **94**, 1339–1360 (2013).
53. Chang, P. et al. An unprecedented set of high-resolution Earth system simulations for understanding multiscale interactions in climate variability and change. *J. Adv. Model Earth Syst.* **12**, e2020MS002298 (2020).
54. Small, R. J. et al. A new synoptic scale resolving global climate simulation using the Community Earth System Model. *J. Adv. Model. Earth Syst.* **6**, 1065–1094 (2014).
55. Hoskins, B. J. & Hodges, K. I. New perspectives on the Northern Hemisphere winter storm tracks. *J. Atmos. Sci.* **59**, 1041–1061 (2002).
56. Hotta, D. & Nakamura, H. On the significance of the sensible heat supply from the ocean in the maintenance of the mean baroclinicity along storm tracks. *J. Clim.* **24**, 3377–3401 (2011).
57. Sampe, T., Nakamura, H., Goto, A. & Ohfuchi, W. Significance of a midlatitude SST frontal zone in the formation of a storm track and an eddy-driven westerly jet. *J. Clim.* **23**, 1793–1814 (2010).
58. Brayshaw, D. J., Hoskins, B. & Blackburn, M. The basic ingredients of the North Atlantic storm track. Part II: sea surface temperatures. *J. Atmos. Sci.* **68**, 1784–1805 (2011).
59. Saulière, J., Brayshaw, D. J., Hoskins, B. & Blackburn, M. Further investigation of the impact of idealized continents and SST distributions on the Northern Hemisphere storm tracks. *J. Atmos. Sci.* **69**, 840–856 (2012).
60. Graff, L. S. & LaCasce, J. H. Changes in the extratropical storm tracks in response to changes in SST in an AGCM. *J. Clim.* **25**, 1854–1870 (2012).
61. O'Reilly, C. H., Minobe, S. & Kuwano-Yoshida, A. The influence of the Gulf Stream on wintertime European blocking. *Clim. Dyn.* **47**, 1545–1567 (2016).
62. Ma, X. et al. Importance of resolving Kuroshio front and eddy influence in simulating the North Pacific storm track. *J. Clim.* **30**, 1861–1880 (2017).

63. Sheldon, L. et al. A 'warm path' for Gulf Stream–troposphere interactions. *Tellus A Dyn. Meteorol. Oceanogr.* **69**, 1299397 (2017).
64. Kwon, Y.-O. et al. Role of the Gulf Stream and Kuroshio–Oyashio systems in large-scale atmosphere–ocean interaction: a review. *J. Clim.* **23**, 3249–3281 (2010).
65. Small, R. J., Msadek, R., Kwon, Y.-O., Booth, J. F. & Zarzycki, C. Atmosphere surface storm track response to resolved ocean mesoscale in two sets of global climate model experiments. *Clim. Dyn.* **52**, 2067–2089 (2019).
66. Brayshaw, D. J., Hoskins, B. & Blackburn, M. The Storm-Track Response to Idealized SST Perturbations in an Aquaplanet GCM. *J. Atmos. Sci.* **65**, 2842–2860 (2008).
67. O'Neill, L. W., Chelton, D. B. & Esbensen, S. K. Observations of SST-induced perturbations of the wind stress field over the Southern Ocean on seasonal timescales. *J. Clim.* **16**, 2340–2354 (2003).
68. Chelton, D. B., Schlax, M. G., Samelson, R. M. & de Szoeke, R. A. Global observations of large oceanic eddies. *Geophys. Res. Lett.* **34**, 2007GL030812 (2007).
69. Xie, S.-P. Satellite observations of cool ocean–atmosphere interaction. *Bull. Am. Meteorol. Soc.* **85**, 195–208 (2004).
70. Risien, C. M. & Chelton, D. B. A global climatology of surface wind and wind stress fields from eight years of QuikSCAT scatterometer data. *J. Phys. Oceanogr.* **38**, 2379–2413 (2008).
71. Small, R. J. et al. Air–sea interaction over ocean fronts and eddies. *Dyn. Atmos. Oceans* **45**, 274–319 (2008).
72. Brachet, S. et al. Atmospheric circulations induced by a midlatitude SST front: a GCM study. *J. Clim.* **25**, 1847–1853 (2012).
73. O'Neill, L. W., Chelton, D. B. & Esbensen, S. K. The effects of SST-induced surface wind speed and direction gradients on midlatitude surface vorticity and divergence. *J. Clim.* **23**, 255–281 (2010).
74. O'Neill, L. W., Haack, T., Chelton, D. B. & Skyllingstad, E. The Gulf Stream convergence zone in the time-mean winds. *J. Atmos. Sci.* **74**, 2383–2412 (2017).
75. Putrasahan, D. A., Miller, A. J. & Seo, H. Isolating mesoscale coupled ocean–atmosphere interactions in the Kuroshio Extension region. *Dyn. Atmos. Oceans* **63**, 60–78 (2013).
76. Vannière, B., Czaja, A., Dacre, H. & Woollings, T. A "cold path" for the Gulf Stream–troposphere connection. *J. Clim.* **30**, 1363–1379 (2017).
77. Elson, P. et al. SciTools/cartopy: v.0.22.0. *Zenodo* https://doi.org/10.5281/zenodo.1182735 (2023).
78. Larson, J. Signature of the western boundary currents in local climate variability. https://doi.org/10.17605/OSF.IO/M84U2 (OSF, 2024).

Acknowledgements We thank R. J. Wills, M. Alexander and the anonymous reviewers for their comments on the paper. We thank L. Sun for his assistance with the numerical output and comments on the figures and methods. We thank R. Justin Small and Y.-O. Kwon for the conversations and comments on the results. J.G.L., D.W.J.T. and J.W.H. are supported by the National Science Foundation (grant no. AGS-2055121). D.W.J.T. is supported by the National Aeronautics and Space Administration (NASA) under 80NSSC23K0113 and the NSF CLD Program under AGS-2116186. The analysis and simulations benefited from the high-performance computing support from Casper (https://arc.ucar.edu/knowledge_base/70549550) carried out in the Computational and Information Systems Laboratory of NSF NCAR.

Author contributions J.G.L., D.W.J.T. and J.W.H. conceived the study and wrote the paper. J.G.L. performed the analysis and generated the figures.

Competing interests The authors declare no competing interests.

Additional information

Supplementary information The online version contains supplementary material available at https://doi.org/10.1038/s41586-024-08019-2.

Correspondence and requests for materials should be addressed to David W. J. Thompson.

Peer review information *Nature* thanks Michael Alexander, Robert Jnglin Wills and the other, anonymous, reviewer(s) for their contribution to the peer review of this work. Peer reviewer reports are available.

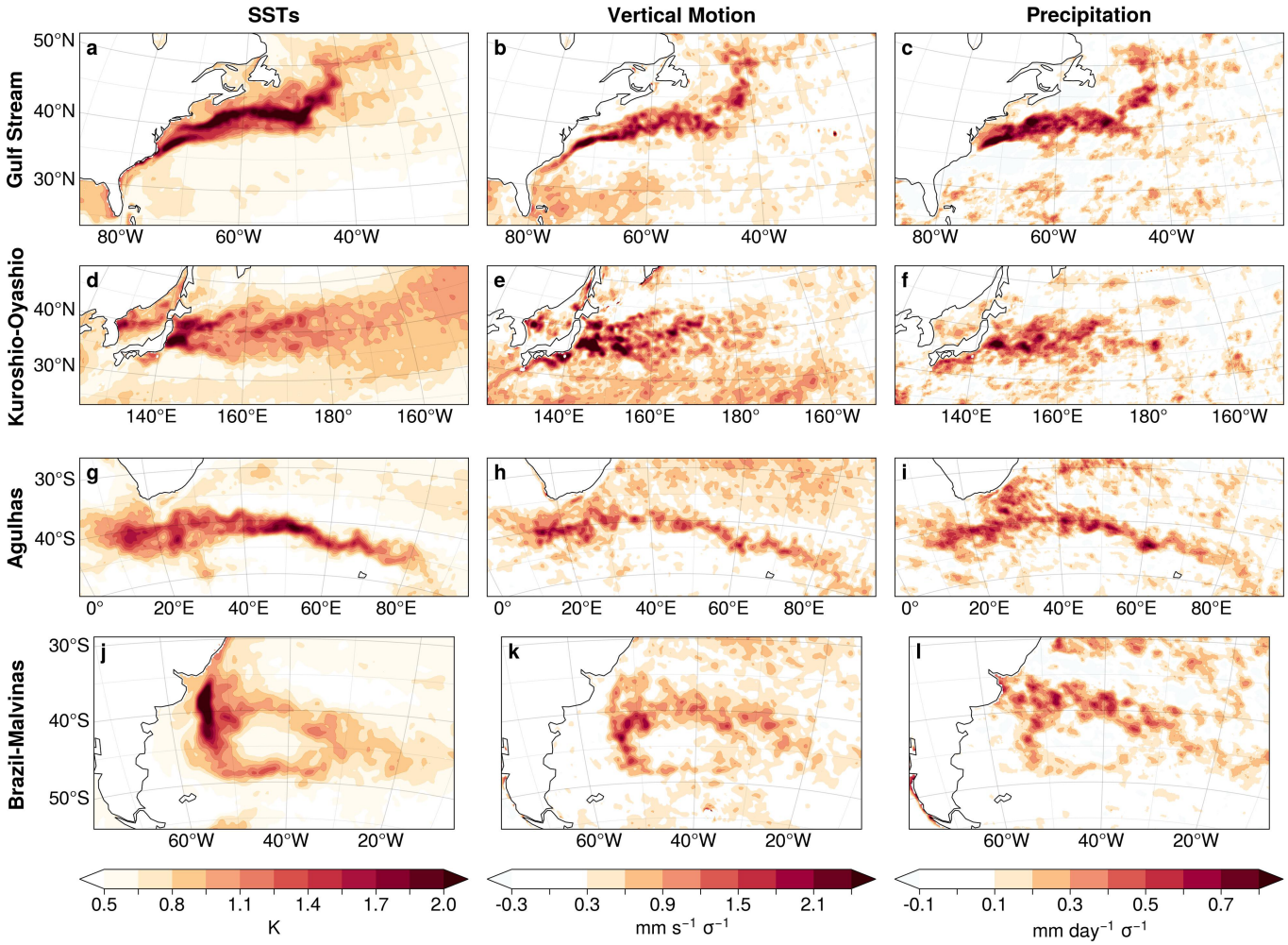

Extended Data Fig. 1 | Signature of western boundary currents in remotely sensed SST and precipitation. (**a, d, g, j**) The standard deviations of monthly grid point SST anomalies; (**b, e, h, k**) grid point vertical motion anomalies at 850 hPa regressed onto grid point SST anomalies; and (**c, f, i, l**) grid point precipitation anomalies regressed onto grid point SST anomalies. The rows correspond to the four western boundary currents of interest. The SST anomalies are based on the National Oceanic and Atmospheric Administration (NOAA) 1/4° Daily Optimum Interpolation Sea Surface Temperature (OISST) dataset, the vertical motion field is based on ERA5, and the precipitation field is based on the National Aeronautics and Space Administration's (NASA) Global Precipitation Measurement Mission (GPM). Each dataset is based on monthly mean output.

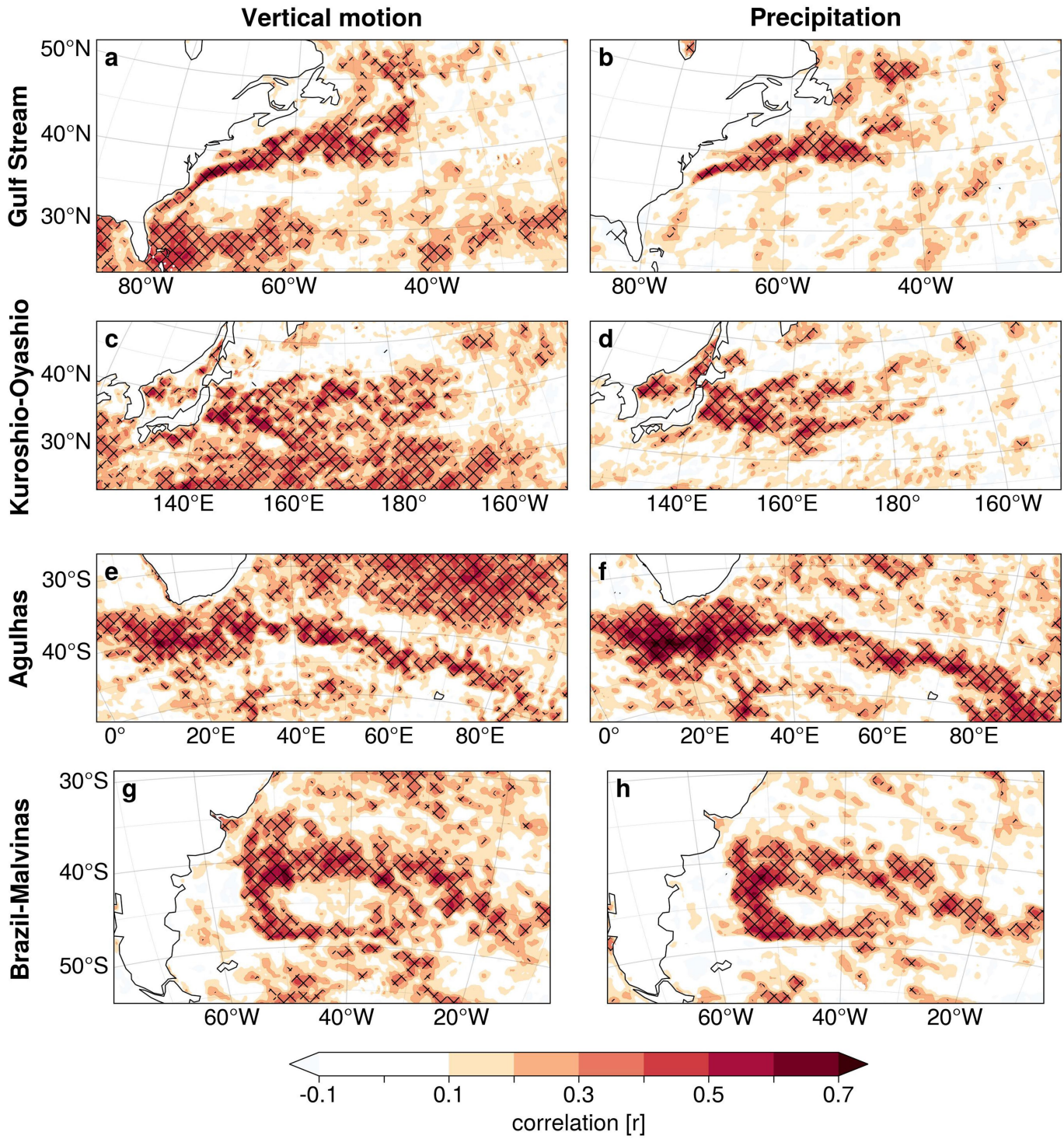

Extended Data Fig. 2 | Statistical significance testing of grid point air-sea correlations. Grid point correlation coefficients of (**a, c, e, g**) vertical motion anomalies at 850 hPa correlated with SST anomalies and (**b, d, f, h**) high-pass spatially filtered precipitation anomalies correlated with SST anomalies. Hatching indicates statistically significant values using a two-tail Student's t-test at 99% confidence with 96 degrees of freedom. See Methods for more details. The rows correspond to the four western boundary currents of interest. Results are based on monthly mean ERA5.

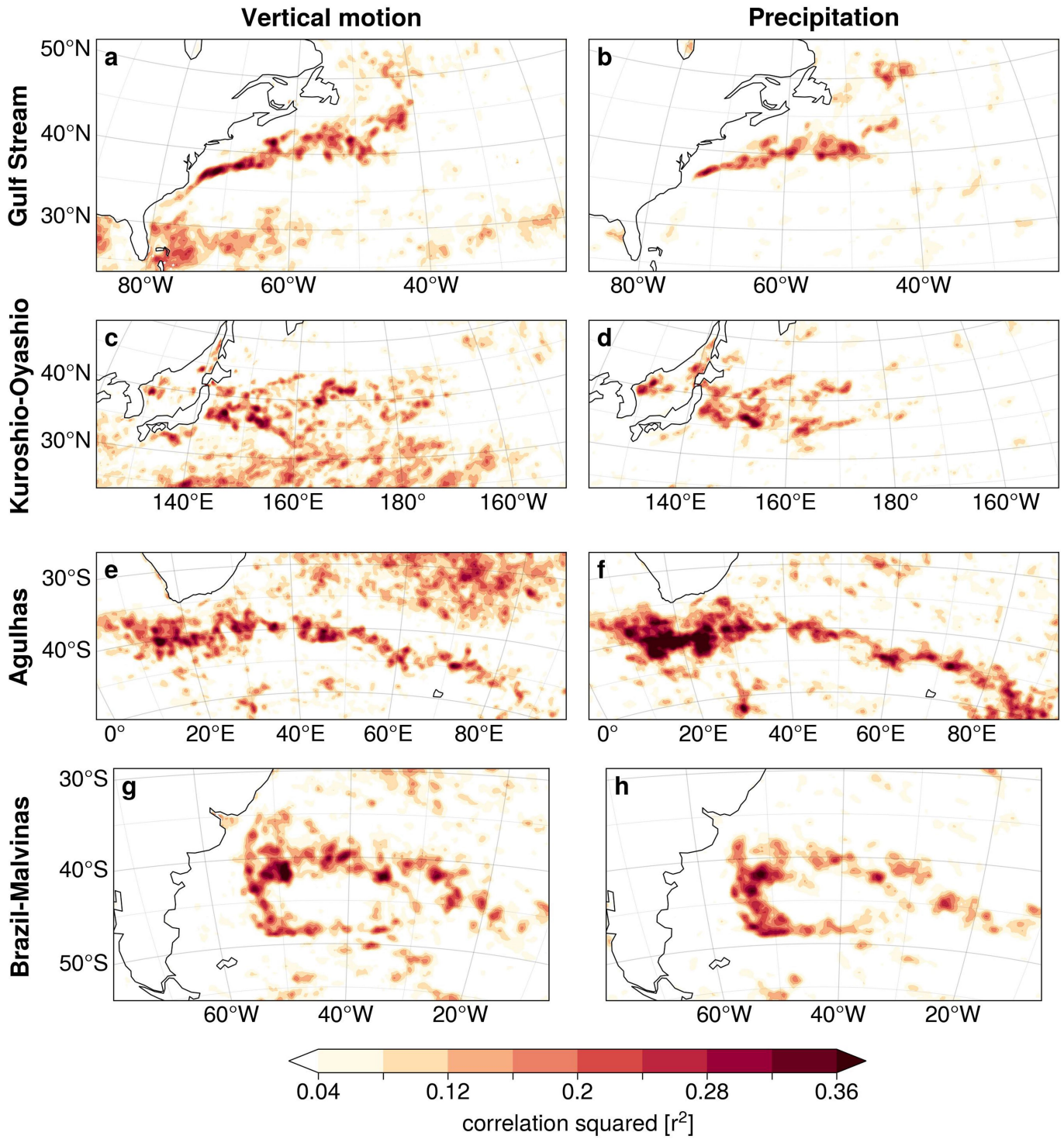

Extended Data Fig. 3 | Variance explained by grid point air-sea correlations. The square of grid point correlation coefficients of (**a, c, e, g**) vertical motion anomalies at 850 hPa correlated with SST anomalies and (**b, d, f, h**) high-pass spatially filtered precipitation anomalies correlated with SST anomalies. See Methods for more details. Results are based on monthly mean ERA5.

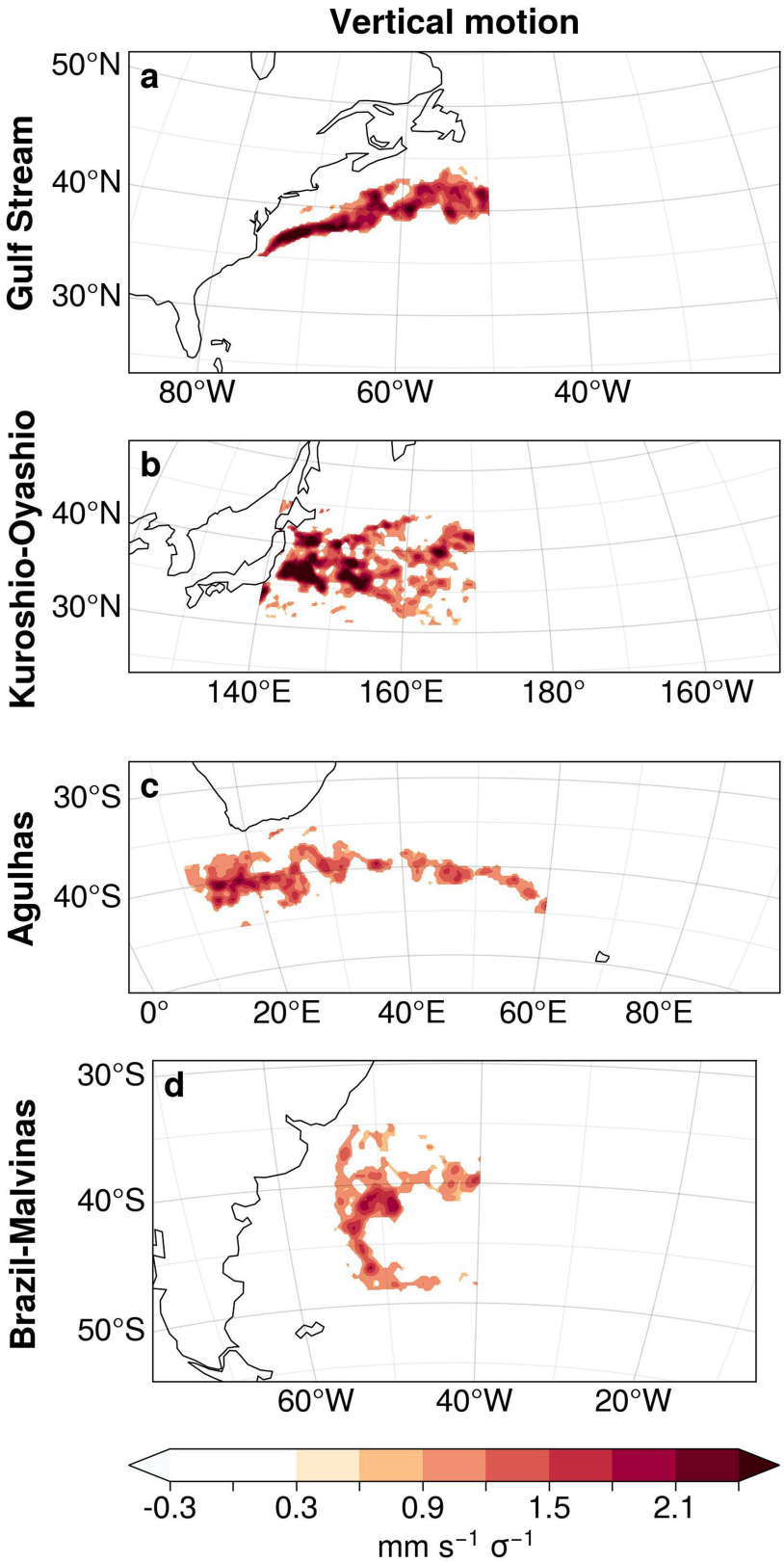

Extended Data Fig. 4 | Spatial masks applied to determine the vertical profile of vertical motion associated with SST variability. The masks, used in the spatial averaging to calculate the results in Fig. 3, exclude all grid points whose regression coefficients of vertical motion at 850 hPa regressed onto SST anomalies fall below the threshold of 0.8 mm s^{-1} σ^{-1} for the (**a**) Gulf Stream, (**b**) Kuroshio-Oyashio Extension, (**c**) Agulhas, and (**d**) Brazil-Malvinas currents. Results are based on monthly mean ERA5.

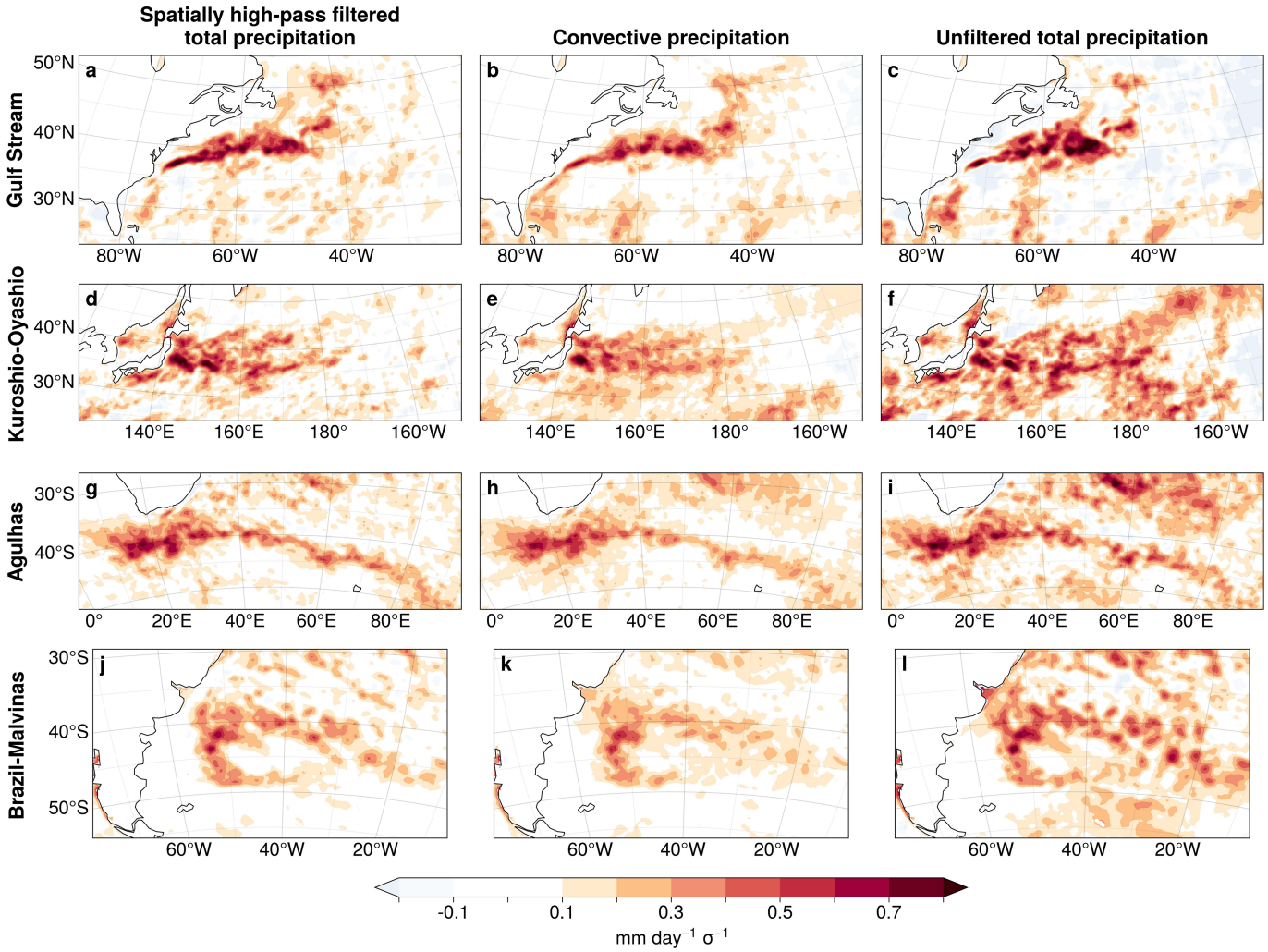

Extended Data Fig. 5 | The effect of high-pass spatial filtering the precipitation field. (**a, d, g, j**) The standard deviations of grid point SST anomalies; (**b, e, h, k**) grid point unfiltered convective precipitation anomalies regressed onto grid point SST anomalies (**c, f, i, l**) grid point unfiltered total precipitation anomalies regressed onto grid point SST anomalies. The rows correspond to the four western boundary currents of interest. Results are based on monthly mean ERA5.

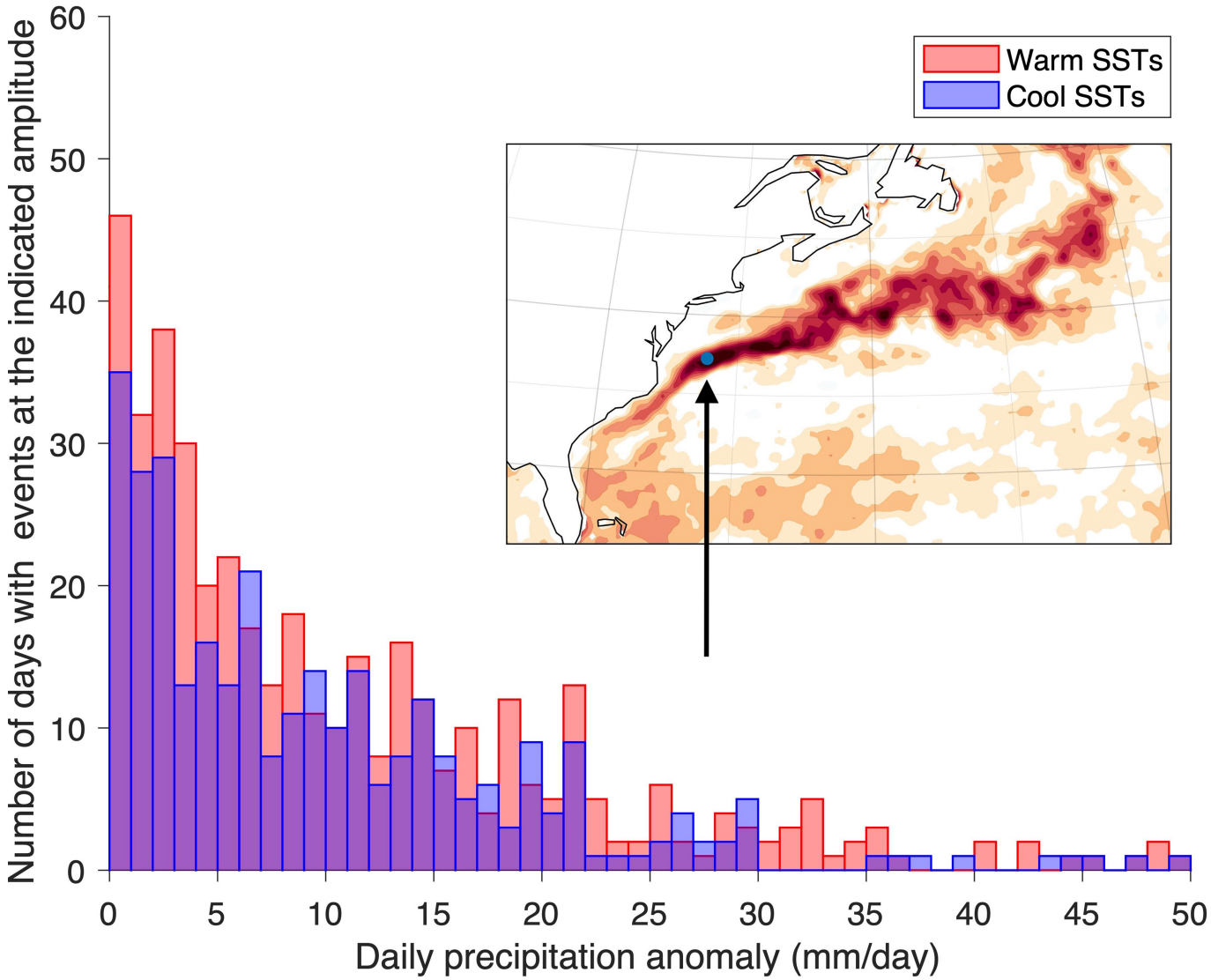

Extended Data Fig. 6 | Composites of daily-mean precipitation during anomalously warm and cold days at a representative location in the Gulf Stream region. The results in Extended Data Fig. 6 explore the signature of the SST field in daily-mean precipitation as a function of precipitation amplitude, and thus indicate whether the covariability observed on month-to-month timescales arises primarily from large amplitude daily precipitation events, or from daily precipitation events across a range of amplitudes. To construct the figure, we: 1) obtained daily values of SST and precipitation (hereafter P) from the grid point identified in the inset in the figure (in the inset, the shading reproduces the vertical motion covariability from Fig. 2 panel b, and the grid point lies in a region of large SST-vertical motion covariability in the Gulf Stream region); 2) removed the seasonal-cycle and long-term trend from the SST data at the selected grid point; 3) formed composites of wintertime precipitation based on days when the SST anomaly time series at the grid point was higher than normal (SST > 1 standard deviation) and lower than normal (SST < −1 standard deviation); and 4) binned the composite precipitation values for warm and cold conditions by the amplitude of the daily-mean precipitation. The analyses are based on ~1300 days in both the SST > 1 standard deviation and SST < −1 standard deviation bins. The bars show the results as histograms, where the x-axis indicates the daily-mean precipitation amplitude and the y-axis indicates the number of days within each precipitation amplitude bin. The key result is that warm days (red bars) are marked by an increased incidence of precipitation events relative to cold days (blue bars) across a range of precipitation amplitudes. That is, they are marked by an increased incidence of not only large-amplitude precipitation events (right part of the plot) but also small amplitude events (left part of the plot). Similar conclusions emerge from analyses at other sample grid points within the different western boundary currents.